

See discussions, stats, and author profiles for this publication at: <https://www.researchgate.net/publication/272381088>

Nitrogen- and Phosphorus-Doped Biocarbon with Enhanced Electrocatalytic Activity for Oxygen Reduction

ARTICLE *in* ACS CATALYSIS · FEBRUARY 2015

Impact Factor: 9.31 · DOI: 10.1021/cs501632y

CITATIONS

9

READS

25

5 AUTHORS, INCLUDING:



Chuying Ouyang

Jiangxi Normal University

105 PUBLICATIONS **1,729** CITATIONS

SEE PROFILE



Ruizhi Yang

Soochow University (PRC)

66 PUBLICATIONS **1,268** CITATIONS

SEE PROFILE

Nitrogen- and Phosphorus-Doped Biocarbon with Enhanced Electrocatalytic Activity for Oxygen Reduction

Xin Gong,^{†,‡} Shanshan Liu,[†] Chuying Ouyang,[‡] Peter Strasser,^{||} and Ruizhi Yang^{*,†}

[†]College of Physics, Optoelectronics and Energy & Collaborative Innovation Center of Suzhou Nanoscience and Technology, Soochow University, Suzhou, Jiangsu 215006, People's Republic of China

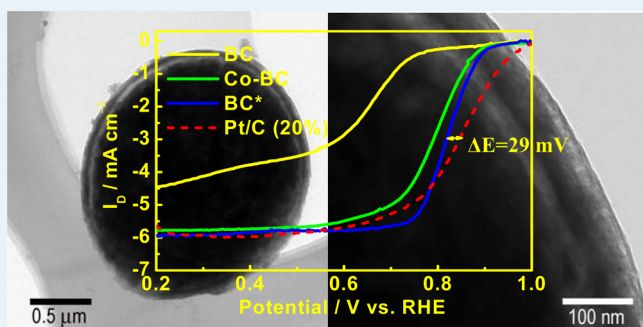
[‡]Department of Physics & Key Laboratory for Advanced Functional Materials of Jiangxi Province, Jiangxi Normal University, Nanchang, Jiangxi 330022, People's Republic of China

^{||}Department of Chemistry, Chemical Engineering Division, Technical University Berlin 10623, Germany

Supporting Information

ABSTRACT: The oxygen reduction reaction (ORR) at the cathode of fuel cells and metal–air batteries requires efficient electrocatalysts to accelerate its reaction rate due to its sluggish kinetics. Nitrogen- and phosphorus-doped biocarbon has been fabricated via a simple and low-cost biosynthesis method using yeast cells as a precursor. The as-prepared biocarbon exhibits excellent electrocatalytic activity for the ORR. An onset potential of -0.076 V (vs Ag/AgCl) and a negative shift of only about 29 mV in the half-wave potential of the biocarbon as compared to commercial Pt/C (20 wt % Pt on Vulcan XC-72, Johnson Matthey) is achieved. The biocarbon possesses enhanced electron poverty in carbon atoms and a decreasing amount of less electroactive nitrogen and phosphorus dopants due to the biomineralization during the synthesis. The surface gap layer along with the mesopores in the biocarbon increases accessible active sites and facilitates the mass transfer during the ORR. These factors correlate with the high ORR activity of the biocarbon. The results demonstrate that biomineralization plays a critical role in tailoring the structure and the electrocatalytic activity of the biocarbon for ORR.

KEYWORDS: biocarbon, yeast cells, nitrogen- and phosphorus-doped, electrocatalytic activity, oxygen reduction reaction



INTRODUCTION

The increasing demand for environmentally friendly energy sources with high energy density has promoted global research interest in fuel cells and metal–air batteries.^{1–3} The performance of fuel cells and metal–air batteries is limited by the slow kinetics of the cathodic oxygen reduction reaction (ORR).^{2–4} Platinum-based electrocatalysts have been widely investigated for the ORR. However, the high cost and poor long-term operational stability of platinum are the main barriers to the widespread commercialization of fuel cells and metal–air batteries. The development of low-cost and efficient catalysts for ORR is highly desirable.^{3–6}

In recent years, heteroatom-doped carbon materials, as alternatives to noble-metal catalysts, have attracted much attention due to their greater abundance, lower price, and higher catalytic activity toward ORR.^{7–14} Doping the carbon materials with heteroatoms, such as nitrogen (N),^{8–12} boron (B),^{7,10,13,14} sulfur (S),^{15–17} and phosphorus (P),^{18–22} has been reported to improve the ORR activity of carbon. Doping-induced atomic charge density and/or spin density redistribution has been proved to be favorable for O₂ adsorption and facilitating ORR.^{9,14,23–26} Recent pioneering works have shown that codoping of carbon with binary or ternary heteroatoms

shows even higher catalytic activity than single-atom doping due to a synergetic effect arising from codoping of more than one heteroatom in carbon.^{7,24,27–30} Various state-of-the-art techniques have been developed to prepare heteroatom-doped carbon catalysts. However, these methods often involve environmentally hazardous precursors and a tedious and/or expensive preparation process. Alternative eco-friendly and simple methods are needed for the fabrication of heteroatom-doped carbon with a significantly improved electrocatalytic activity for ORR.^{9,31}

In this work, we report for the first time a facile, energy-efficient biosynthesis method using yeast cells as a precursor to prepare highly active nitrogen- and phosphorus-doped biocarbon for ORR. In comparison with conventional synthesis methods, the advantage of the biosynthesis method is that advanced materials can be synthesized in an environmentally friendly system. Moreover, the structure and morphology of the materials can be easily controlled by tuning the biosynthetic conditions.^{32,33} Yeast cells are a kind of microorganism with a

Received: August 15, 2014

Revised: December 22, 2014

large surface area and abundant surface charge in a wide range of pHs. They can accumulate metal ions from aqueous solutions via a self-assembly process to produce minerals: i.e., so-called biomineralization. With this biomineralization process, the structure of the synthetic materials can be controlled at a molecular level. In addition, yeast cells have the advantage of being low cost, nontoxic, and easily scaled up. The excellent electrocatalytic activity of the yeast cell derived nitrogen- and phosphorus-doped biocarbon for the ORR in alkaline media has been demonstrated, which renders this material a very good electrocatalyst candidate for fuel cell and metal–air applications.

EXPERIMENTAL SECTION

Sample Preparation. Nitrogen- and phosphorus-doped carbon was prepared by a biosynthesis method. In a typical experiment, 10 g of instant dry yeast was cultivated in 1000 mL of glucose aqueous solution (0.01 g mL^{-1}) for 30 min at 30°C . The purified yeast cells were obtained by centrifugation and washing with ultrapure water and were then dissolved in deionized water (1000 mL) to form a uniform bioemulsion. Afterward, 0.121 g of $\text{Co}(\text{NO}_3)_2 \cdot 6\text{H}_2\text{O}$ ($\geq 99.0\%$, Sinopharm Chemical Reagent Co. Ltd.) was added to the bioemulsion with stirring at room temperature overnight for biomineralization. Then the suspension was transferred to a lyophilizer and dried at -47°C for 24 h to avoid the agglomeration of yeast cells. The dried powder was loaded into a graphite boat and then pyrolyzed under N_2 at 800°C for 2 h. The obtained Co-containing mineral–biocarbon composites are denoted as Co-BC. Half of the composites was stirred in 500 mL of 1.0 M HCl solution for 12 h to dissolve the Co-based mineral in the biocarbon. Finally, the samples were washed with ultrapure water until neutral pH was reached and dried in an oven at 90°C followed by heat treatment under N_2 at 800°C for 1 h. The samples obtained are denoted as BC*. The pure biocarbon was also prepared by using a similar heat-treatment process with purified yeast cells as precursors for comparison, which is denoted as BC.

Electrochemical Measurements. The electrocatalytic activity of the samples for the ORR was studied with a rotating ring–disk electrode (RRDE) technique, where a Pine electrochemical system (AFMSRX rotator, and AFCBP1 bipotentiostat) was used. The RRDE electrode consisted of a catalyst-coated glassy-carbon (GC) disk (5 mm diameter, 0.196 cm^2 of geometric surface area) surrounded by a Pt ring (6.5 mm inner diameter, 7.6 mm outer diameter, 0.125 cm^2 of geometric surface area). The electrochemical measurements were conducted in a standard three-electrode electrochemical cell at 25°C . Pt foil was used as the counter electrode, and an Ag/AgCl (3 M Cl^- , Cypress) reference electrode was used in a double-junction reference chamber. The potential of the Ag/AgCl reference electrode was calibrated versus the reversible hydrogen electrode (RHE). The potentials reported in this work all refer to the RHE potential. The electrolyte was 0.1 M KOH solution prepared from ultrapure water (Millipore, $18.2 \text{ M}\Omega \text{ cm}$). The catalyst inks were prepared by mixing 10 mg of catalyst powder, 10 μL of Nafion solution (5 wt % from Aldrich), and 700 μL of ethanol. The catalyst loading on the GC disk was $503 \mu\text{g cm}^{-2}$. The loading of the commercial Pt/C (20 wt % Pt on Vulcan XC-72, Johnson Matthey) is the same.

For the ORR test, linear sweep voltammetry (LSV) measurements were performed in O_2 -saturated 0.1 M KOH by sweeping the potential from -0.9 V anodically to 0 V at 10

mV s^{-1} with the electrode rotated at 400, 900, 1600, and 2500 rpm. The ring potential was held at 0.5 V vs Ag/AgCl in order to oxidize any H_2O_2 produced in alkaline solution.³⁴ For each catalyst tested, the background current (the current measured from the cyclic voltammograms under Ar) has been subtracted from the ORR data.

The kinetic current density for the ORR was derived from the Koutecky–Levich equation:

$$1/j = 1/j_k + 1/j_d = 1/j_k + 1/(B\omega^{1/2}) \quad (1)$$

where j is the measured disk current density; j_k and j_d are the kinetic and diffusion limiting current densities, respectively, and B is the Levich slope, which is given by the equation

$$B = 0.62nFD_{\text{O}_2}^{2/3}\nu^{-1/6}C_{\text{O}_2} \quad (2)$$

where n is the apparent number of electrons transferred in the reaction, F is the Faraday constant (96485 C mol^{-1}), D_{O_2} is the diffusion coefficient of O_2 ($D_{\text{O}_2} = 1.86 \times 10^{-5} \text{ cm}^2 \text{ s}^{-1}$), ν is the kinematic viscosity of the solution ($\nu = 0.01 \text{ cm}^2 \text{ s}^{-1}$), C_{O_2} is the concentration of O_2 dissolved in electrolyte ($C_{\text{O}_2} = 1.21 \times 10^{-6} \text{ mol cm}^{-3}$),^{35,36} and ω is the electrode rotation speed (rad s^{-1}). The ohmic resistances in the electrode contacts and electrolyte solution were assumed to be the same for the samples and were not included in the corrections.

The % HO_2^- produced during the reaction was calculated using the equation^{37–39}

$$\% \text{HO}_2^- = 100 \frac{2I_R/N}{I_D + (I_R/N)} \quad (3)$$

where I_D is the Faradaic current at the disk, I_R is the Faradaic current at the ring, and $N = 0.22$ is the disk electrode collection efficiency.

Physical Characterization. The crystal structure of the sample was determined with X-ray diffraction (XRD) using a Bede D1 X-ray diffractometer (UK, Bede Scientific Ltd.; Cu $K\alpha$ radiation; $\lambda = 0.15418 \text{ nm}$).

The element binding environment of the samples was analyzed with an X-ray photoelectron spectroscopy spectrometer (XPS, VG ESCALAB MKII). The spectra were corrected for background using the Shirley approach, and the surface composition of the samples was determined by measuring the ratio of C 1s to N 1s or P 2p intensities (integrated peak area) normalized by their respective sensitivity factors.^{40,41}

The specific surface area and the pore size distribution of the samples were analyzed from nitrogen sorption isotherms that were performed on a BEL-SORPmini system (BEL Japan).

The morphology and microstructure of the synthesized sample were characterized by a scanning electron microscope (SEM, Hitachi S4700) and a transmission electron microscope (TEM, TecnaiG220 operating at 200 kV). The d spacing of the sample was determined using Digital Micrograph software. Specifically, with this software, the high-resolution transmission electron microscope (HRTEM) image of the sample was filtered and the fast Fourier transform (FFT) pattern of the HRTEM image was obtained. The d spacing value was determined by an analysis of the FFT pattern.

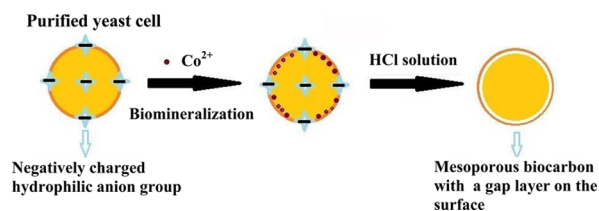
The contents of P and residual metal in the biocarbon were measured with inductively coupled plasma atomic emission spectroscopy (ICP-AES) (Vista MPX). The content of N in the

biocarbon was measured with an elemental analyzer (EA 3000, Euro Vector).

RESULTS AND DISCUSSION

Synthesis and Characterization of Nitrogen- and Phosphorus-Doped Biocarbon. The preparation of nitrogen- and phosphorus-doped biocarbon is shown in Scheme 1.

Scheme 1. Illustration of the Synthesis of Biocarbon



The hydrophilic anion groups exist on the cell wall surface after the cultivation of yeast cells. When $\text{Co}(\text{NO}_3)_2 \cdot 6\text{H}_2\text{O}$ is added to the purified yeast solution, Co^{2+} cations combine with the hydrophilic anion groups (such as $-\text{OH}^-$, $-\text{COO}^-$, and $-\text{OPO}_3^{2-}$) and amide group on the surface of the yeast cells by electrostatic and chemical interaction.^{42,43} The Co-based mineral is formed and self-assembles on the yeast cell wall surface via a biomineralization process. The following heat treatment at 800 °C in Ar resulted in the formation of Co-containing mineral–biocarbon composites (Co-BC). After the removal of Co-containing mineral with HCl solution, mesoporous biocarbon (BC*) containing both nitrogen and phosphorus with a gap layer on the surface is produced.

The microstructures of BC, Co-BC, and BC* were characterized by transmission electron microscopy (TEM). As

can be seen in Figure 1a,b, nanoparticles are formed on the surface of biocarbon after the adsorption of Co^{2+} . The HRTEM images (Figure 1c,d) combined with the XRD pattern (Figure 2a) of Co-BC reveal that these nanoparticles are NH_4CoPO_4 : i.e., a Co-containing mineral. The lattice fringes of Co-BC correspond to d space values of 0.628 (Figure 1c) and 0.436 and 0.271 nm (Figure 1d), which are in good agreement with the d space values revealed in the XRD pattern of NH_4CoPO_4 (PDF# 22-0042, Figure 2a). These results clearly show that, upon the adsorption of Co^{2+} , NH_4CoPO_4 is formed on the surface of yeast cells via a biomineralization process. The N and P in yeast cells exist in the form of amide and $-\text{OPO}_3^{2-}$, respectively. The N and P content in yeast cells determined with the Kjeldahl method and spectrophotometry are 8.67% and 1.04%, respectively. The electrostatic interaction between Co^{2+} and $-\text{OPO}_3^{2-}$ and chemical interaction between Co^{2+} and the amide group result in the formation of NH_4CoPO_4 during the biomineralization process. Moreover, the NH_4CoPO_4 nanoparticles are surrounded by amorphous carbon (Figure 1c,d), indicating successful embedding of these nanoparticles in the surface of biocarbon. After washing with HCl, a gap layer with a width of about 20–50 nm is formed on the surface of biocarbon (Figure 1e,f) due to the removal of NH_4CoPO_4 nanoparticles embedded in the surface. The final biocarbon is amorphous, as revealed by the XRD pattern (Figure 2a) and SAED pattern (Figure 1f) of BC*.

The surface area and porosity of the catalysts were studied by means of nitrogen sorption techniques (Figure 2b). The nitrogen adsorption–desorption isotherms of all samples show distinct hysteresis loops at medium- and high-pressure ($P/P_0 = 0.5\text{--}1.0$) regions, which are attributed to the mesopores in the bulk and macropores formed in the gap layer on the surface of

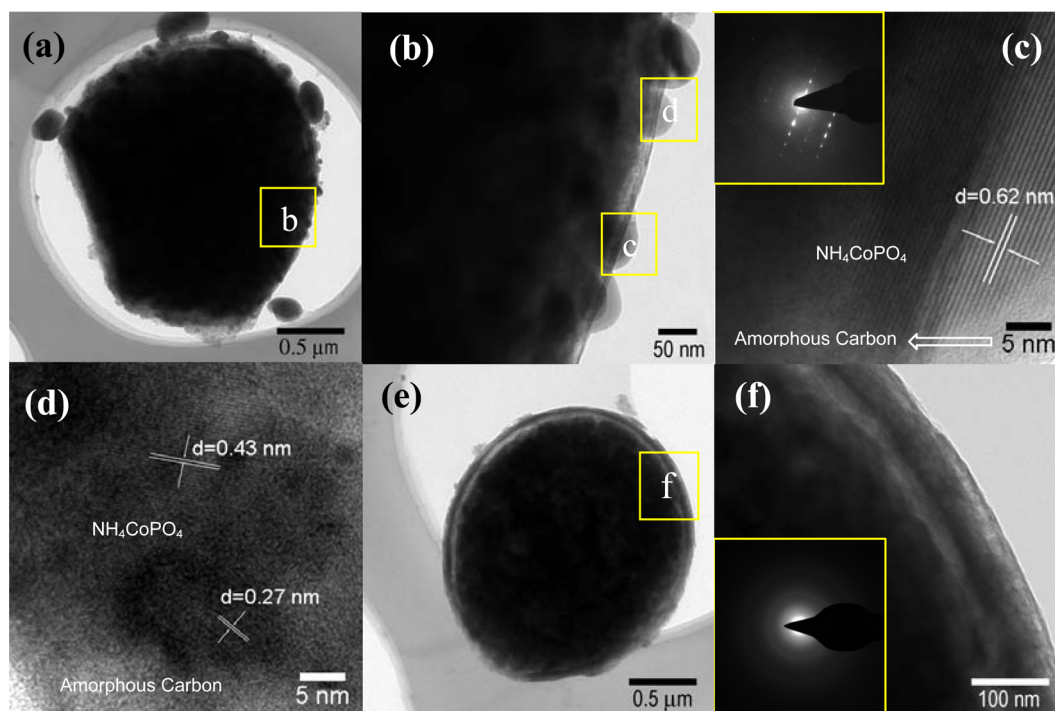


Figure 1. (a) TEM image of Co-BC (magnification $\times 6000$). (b) High-magnification ($\times 50000$) TEM image of Co-BC in the corresponding region of (a). (c,d) HRTEM images (magnification $\times 500000$) of Co-BC in the corresponding region of (b) and SAED pattern (inset) of Co-BC. (e) TEM images of BC* (magnification $\times 6000$). (f) High-magnification ($\times 38000$) TEM image of BC* in the corresponding region of (e) and SAED pattern (inset) of BC*.

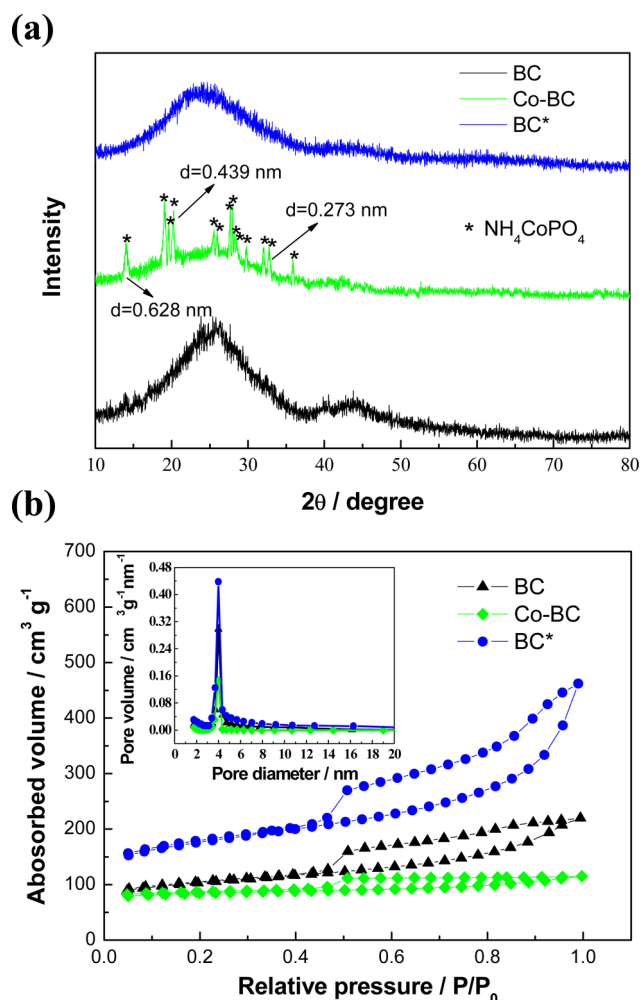


Figure 2. (a) XRD patterns of BC, Co-BC, and BC*. (b) BET surface area and pore size distribution (inset) of BC, Co-BC, and BC*.

BC*. As shown in the inset of Figure 2b, the diameter of mesopores determined by the Barrett–Joyner–Halenda (BJH) method is ca. 4 nm. BC, Co-BC, and BC* have identical pore size distributions. BC exhibits 332.8 m² g⁻¹ of BET specific surface area. After the formation of NH₄CoPO₄ on the surface, the specific surface area decreases to 260.0 m² g⁻¹ because of partial blocking of mesopores by NH₄CoPO₄. In contrast, the specific surface area increases to 575.3 m² g⁻¹ after acid washing due to the removal of NH₄CoPO₄ and the formation of a gap layer in the surface of BC*. The gap layer formed on the surface and the mesopores in the sample increase the number of accessible active sites and facilitate the mass transfer inside this material.

The chemical environment of elements in the materials has been investigated by X-ray photoelectron spectroscopy (XPS). The survey scan shows similar element species of C, N, and P in all samples and Co species in Co-BC (Figure 3a). The Co 2p spectrum indicates the presence of Co²⁺ in Co-BC (Figure S1, Supporting Information). Note that Co was completely washed off, as indicated by the absence of a Co signal in the XPS survey scan of BC* (Figure 3a). Moreover, the TGA analysis of the sample (Figure S2, Supporting Information) has shown that the sample is burned off completely after ca. 750 °C in air. The ICP-AES measurement on the sample has shown that the Co content in BC* is 0.03 wt %. The TGA and ICP-AES results

further confirm that BC* is Co-free. High-resolution XPS scans of N 1s in BC* (Figure 3b) show that the N 1s spectrum can be deconvoluted into two N species (N1 and N2) centered at ca. 400.7 and 398.3 eV, corresponding to pyrrolic N and pyridinic N, respectively.^{44,45} As can be seen from Figure 3b, the pyrrolic N content does not change much upon the adsorption of Co²⁺ and subsequent formation of NH₄CoPO₄ in Co-BC (53.45% for BC and 52.83% for Co-BC). Remarkably, after the removal of NH₄CoPO₄ with HCl, the pyrrolic N content decreases to 45.59% (Figure 3b). This clearly indicates that Co²⁺ mostly binds to pyrrolic N in the formation of NH₄CoPO₄. The high-resolution P 2p spectrum (Figure 3c) can also be deconvoluted into two P species (P1 and P2) centered at ca. 134.4 and 133.1 eV, which are assigned to P–O and P–C bonds, respectively.^{46–48} Similarly, not much change has been observed for the P–O and P–C content upon the formation of NH₄CoPO₄ in Co-BC. However, oxidized P species (i.e., P–O bond) decreases from 49.75 to 40.47% after the removal of NH₄CoPO₄ (Figure 3c), suggesting that oxidized P species participated in the formation of NH₄CoPO₄. Meanwhile, the overall N and P contents in the biocarbon decrease from 6.29% and 2.62% to 5.16% and 1.94% after acid washing, as confirmed by elemental analysis and ICP-AES measurements, respectively. Note that the forms of N and P existing in the biocarbon (BC) are different from those existing in the precursor yeast cells (amide and –OPO₃^{2–}) due to the biomineralization and subsequent pyrolysis. Meanwhile, as the yeast cells turn into biocarbon, the overall N content decreases from 8.67% to 6.29% due to partial loss of N^{49,50} and the P content increases from 1.04% to 2.62% due to partial loss of H, O, C, and N after pyrolysis at 800 °C under N₂.^{51,52} It is reported that N and P codoping can introduce the charge delocalization and asymmetric spin density of carbon atoms, which contribute to the kinetics enhancement of the ORR.^{24,27,53,54} Note that P-doping itself can not only improve the activity of biocarbon but also bring out the synergistic effect between N–C and P–C bonds, which further promotes the catalytic activity of biocarbon toward ORR.^{24,27,53} Furthermore, this enhancement depends on the type of N and P dopant. Pyridinic N^{8,9,11} and P–C phases^{15,18–20} are reported to be favorable for the ORR. As analyzed from Figure 3b,c, the less active pyrrolic N and oxidized P participated in the formation of NH₄CoPO₄ during the biomineralization. Therefore, more active pyridinic nitrogen and P–C phases are left in the biocarbon, although the overall N and P content in the samples decreases. High-resolution XPS scans of C 1s (Figure 3d) show that the binding energy of C 1s moves up 0.21 eV upon the formation of NH₄CoPO₄ in Co-BC in comparison with BC, which indicates the electron poverty in carbon atoms.²⁸ Due to the difference in the valence states of O in NH₄CoPO₄ and –OPO₃^{2–}, the formation of NH₄CoPO₄ from the electrostatic interaction between Co²⁺ and –OPO₃^{2–} needs extra electrons, which most likely comes from the upshifting in binding energy of C–C bonds. Note that the electron poverty in carbon atoms does not change after the removal of NH₄CoPO₄ (i.e., BC*).

Electrochemical Properties of Nitrogen- and Phosphorus-Doped Biocarbon. To assess the ORR catalytic activity of these biocarbon materials, linear sweep voltammetry (LSV) measurements on all the samples as well as the commercial Pt/C (20 wt %) have been performed with RRDE. The disk currents were measured at 1600 rpm and normalized by the geometric surface area. It can be seen from Figure 4a that BC shows an onset potential of ca. 0.77 V. After a

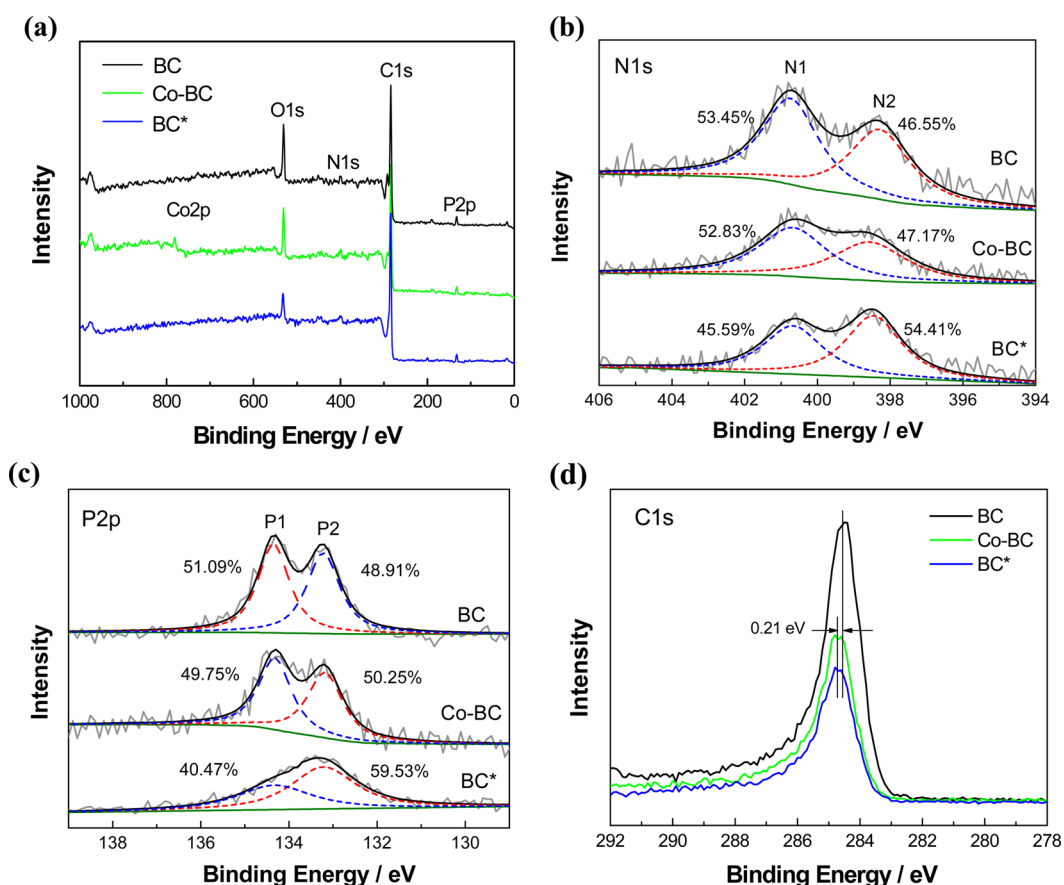


Figure 3. (a) XPS survey scan for BC, Co-BC, and BC*. (b) XPS spectra for N 1s of BC, Co-BC, and BC*. (c) XPS spectra for P 2p of BC, Co-BC, and BC*. (d) XPS spectra for C 1s of BC, Co-BC, and BC*.

biomineralization process, that is the formation of NH_4CoPO_4 , the onset potential of biocarbon (i.e., Co-BC) increases to 0.88 V and the diffusion limiting current density reaches that of Pt/C. When the NH_4CoPO_4 was washed off with HCl, the onset potential increases further to 0.93 V and a negative shift of only about 29 mV exists in the half-wave potential of BC* in comparison to Pt/C. It should be noted that the diffusion limiting current density and half-wave potential of the Pt/C are in good agreement with the values of Pt/C (20 wt % Pt) reported elsewhere.^{55,56} Moreover, the onset potential of BC* is comparable to that of N and P dual-doped hierarchical porous carbon foams (ca. -0.030 V vs Ag/AgCl),⁵³ N and P codoped vertically aligned carbon nanotube arrays (ca. -0.090 V vs SCE),²⁷ and N and P codoped porous carbon derived from MOFs (ca. -0.065 V vs Ag/AgCl)⁵⁴ reported in the literature. The effect of heat-treatment temperature on the ORR activity of BC* was also investigated. As can be seen in Figure S3 (Supporting Information), BC* obtained at 800 °C exhibits the highest onset potential. Meanwhile, the dependence of the N and P content in BC* on the heat treatment temperature in Table S1 (Supporting Information) shows that the N content decreases as the temperature increases due to the loss of N in the sample.^{49,50} The P content first increases with an increase of temperature up to 800 °C due to the loss of H, O, C, and N^{51,52} and then decreases as the temperature goes to 900 and 1000 °C due to the loss of P.⁵⁷ The highest activity of BC* heated at 800 °C results from the optimized N and P contents in the sample. To verify the ORR catalytic pathways on the catalysts, the formation of peroxide species (HO_2^-)

during the ORR process was monitored with RRDE measurements (Figure 4b). The HO_2^- yield (calculated from eq 3) on BC is in the range of 45–60% over the potential range of 0.8–0.2 V. It decreases to 13.5–22.7% on Co-BC and further decreases to below 15.0% on BC*, which is comparable to that for Pt/C. These results indicate that the formation of NH_4CoPO_4 via a biomineralization process in yeast cells plays a crucial role in improving the catalytic activity of biocarbon. Note that NH_4CoPO_4 is not active for the ORR. Interestingly, upon the formation of NH_4CoPO_4 , the electron poverty in carbon atoms is enhanced due to the electron transfer from carbon, which is confirmed from the upshifting of binding energy of the C–C bond in XPS C 1s spectra (Figure 3d).²⁹ It is known that O_2 adsorption favors the positively charged sites; the enhanced electron poverty in carbon can further weaken the O–O bonding in O_2 . Furthermore, less active pyrrolic N and oxidized P decrease due to their participation in the formation of NH_4CoPO_4 and more active pyridinic N and P–C phases for ORR are left in the biocarbon after a biomineralization process. It is believed that these two factors account for the improvement of the catalytic activity of biocarbon after the formation of NH_4CoPO_4 on the surface (i.e., Co-BC), since NH_4CoPO_4 is not active for ORR and the BET surface area of Co-BC decreases in comparison with BC (Figure 2b). The formation of a gap layer on the surface of BC* after the removal of NH_4CoPO_4 makes more active sites exposed and leads to a further increase of the catalytic activity of biocarbon.

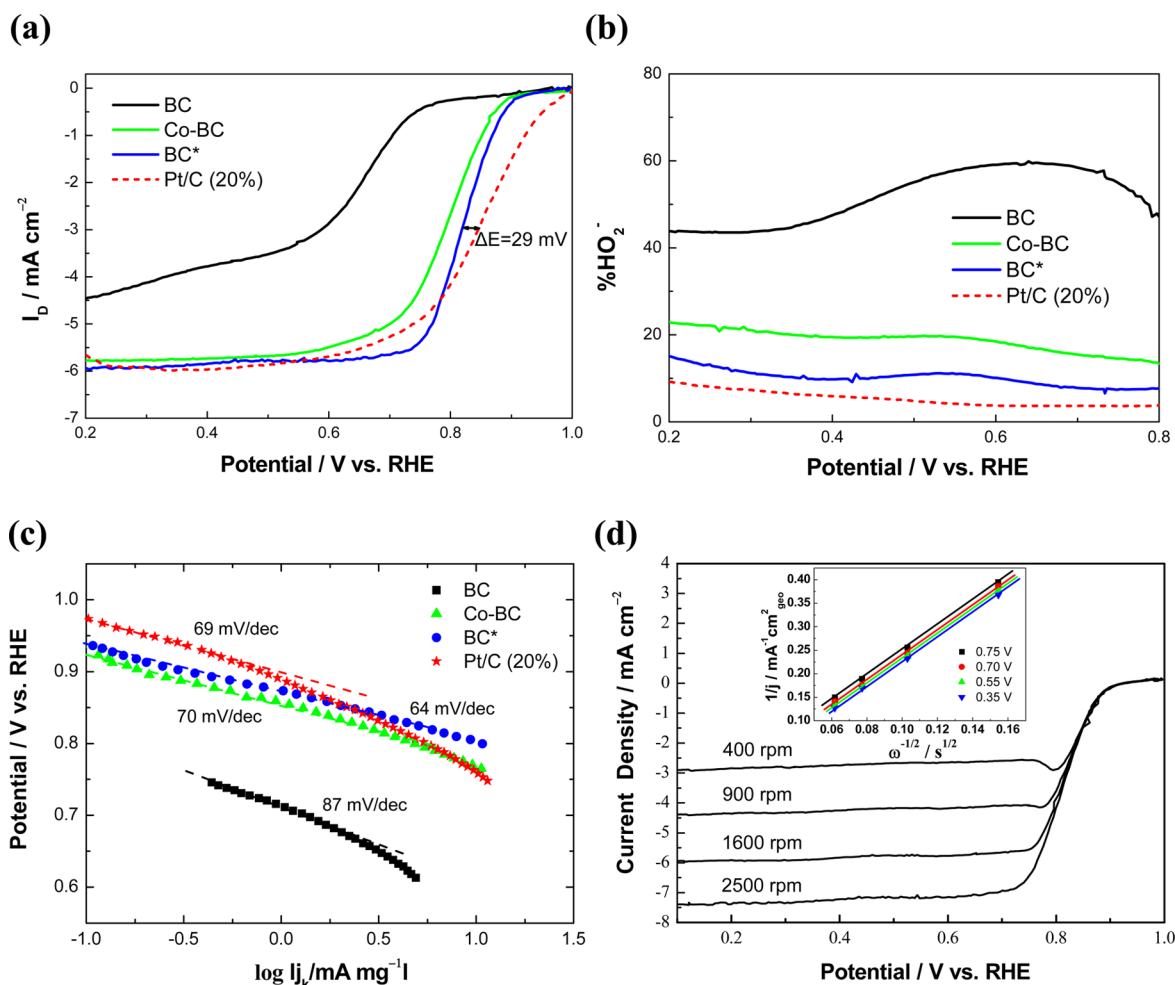


Figure 4. (a) LSVs of ORR on BC, Co-BC, BC* and commercial Pt/C (20 wt % Pt on carbon). (b) % HO_2^- produced during ORR on BC, Co-BC, BC*, and commercial Pt/C (20 wt % Pt on carbon). (c) Tafel plots of BC, Co-BC, BC*, and commercial Pt/C (20 wt % Pt on carbon) derived by the mass transport correction of corresponding LSV data in (a). (d) LSVs of ORR on BC* at different electrode rotating speeds. The inset shows corresponding Koutecky–Levich plots. Measurements in (a)–(d) were made at a sweep rate of 10 mV/s in O_2 -saturated 0.1 M KOH solution at 25 °C.

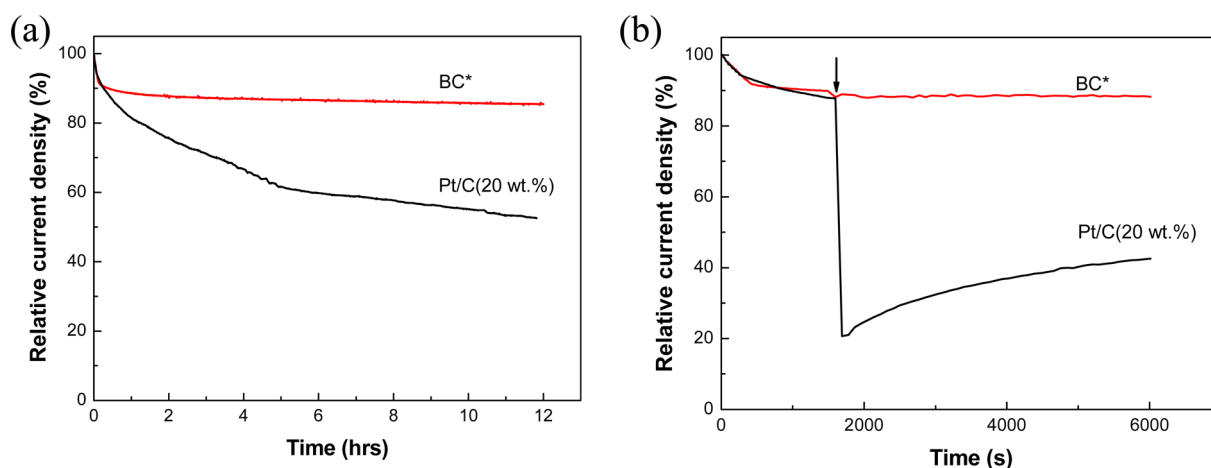


Figure 5. Current–time (i – t) chronoamperometric responses for the ORR on BC* and commercial Pt/C (20 wt % Pt on carbon) in O_2 -saturated 0.1 M KOH at 0.75 V (vs RHE) with a rotating speed of 1600 rpm: (a) stability toward ORR; (b) ethanol crossover tests by introduction of 15 mL of 3.0 M ethanol into the electrolyte at 1600 s. The arrow shows the addition of ethanol into the electrolyte.

The diffusion-current-corrected Tafel plots of specific ORR activity of these samples are shown in Figure 4c. The kinetic currents used for the construction of Tafel plots were derived

from the mass-transport correction using the Koutecky–Levich equation. At low overpotentials, BC* shows a small Tafel slope of 64 mV dec^{-1} , which is smaller than that of Pt/C (69 mV

dec^{-1}) and approaches the theoretical value of $2.303RT/F$ (i.e., 59 mV dec^{-1} at 25°C), where R is the universal gas constant, F is the Faraday constant, and T is the absolute temperature. The Tafel slope of Co-BC is 70 mV dec^{-1} , which is larger than that of Pt/C and that of BC*. However, it is smaller than that of BC (87 mV dec^{-1}). The low Tafel slope indicates the high intrinsic catalytic activity of BC*, since a low Tafel slope means a high intrinsic exchange current density (i.e., a high reaction rate). The decreased Tafel slope with the stepwise preparation process of BC* is related to different active sites as well as the density of active sites for ORR at different stages during the preparation of BC*. The improvements in the catalytic activity of biocarbon, as indicated by Tafel slopes, are in good agreement with the results obtained with RRDE (Figure 4a,b).

The polarization curves for the ORR on BC* at different rotation rates are shown in Figure 4d. They all reached well-defined diffusion limiting currents. The inset of Figure 4d shows the corresponding Koutecky–Levich plots for BC* at 0.75, 0.70, 0.55, and 0.35 V, respectively. These plots are linear and parallel, indicating the first-order dependence of the kinetics of ORR on BC*. The electron transfer number on BC* calculated from the Levich slope ($0.42 \text{ mA cm}^{-2} \text{ rad}^{-1/2} \text{ s}^{1/2}$) based on eqs 1 and 2 is ca. 3.80, indicating a dominant 4e^- reaction pathway for the ORR on BC*.

The stabilities of BC* and commercial Pt/C (20 wt %) were examined with the chronoamperometric method. As shown in Figure 5a, the ORR current density of BC* at 0.75 V decreases by 14.5% after 12 h of continuous operation, while a decrease of 47.2% in the current density is observed for Pt/C. This clearly shows the high durability of BC*, which is attributed to the strong covalent bond between C and N as well as P. The BC* and commercial Pt/C were further subjected to testing the possible crossover of other fuel molecules (e.g., ethanol) as shown in Figure 5b. A sharp decrease in current is observed for the Pt/C electrocatalyst upon addition of 3.0 M ethanol. However, the BC* electrocatalyst does not show obvious change after the addition of ethanol. This indicates that the BC* has higher fuel selectivity toward ORR than the commercial Pt/C.

CONCLUSIONS

In conclusion, nitrogen- and phosphorus-doped biocarbon has been successfully fabricated via a simple and low-cost biosynthesis method. Benefiting from the enhanced electron poverty in carbon atom and a decreasing amount of less active N and P dopants as well as increased accessible active sites and improved mass transfer facilitated by the surface gap layer, the biocarbon exhibits excellent electrocatalytic activity for the ORR. This simple and feasible biosynthesis method offers an opportunity of tuning the structure and electrocatalytic activity of carbon for applications in catalysts, fuel cells and metal–air batteries.

ASSOCIATED CONTENT

Supporting Information

The following file is available free of charge on the ACS Publications website at DOI: 10.1021/cs501632y.

XPS spectra for Co 2p of Co-BC, thermogravimetric analysis of BC*, and the dependence of the ORR activity and the dependence of the N and P content in BC* on the heat treatment temperature (PDF)

AUTHOR INFORMATION

Corresponding Author

*R. Yang: tel, +86-512-65221519; e-mail, yangrz@suda.edu.cn.

Notes

The authors declare no competing financial interest.

ACKNOWLEDGMENTS

This work was supported by the National Natural Science Foundation of China (Nos. 51272167 and 21206101). Part of this work was supported by the Sino-German Network on Electromobility.

REFERENCES

- (1) Dresselhaus, M. S.; Thomas, I. L. *Nature* **2001**, *414*, 332–337.
- (2) Adzic, R. R. In *Electrocatalysis*; Lipkowski, J., Ross, P. N., Eds.; Wiley: New York, 1998; pp 197–242.
- (3) Bruce, P. G.; Hardwick, L. J.; Abraham, K. M. *Mater. Res. Soc. Bull.* **2011**, *36*, 506–512.
- (4) Gasteiger, H. A.; Kocha, S. S.; Sompalli, B.; Wagner, F. T. *Appl. Catal., B* **2005**, *56*, 9–35.
- (5) Yang, R. Z.; Leisch, J.; Strasser, P.; Toney, M. *Chem. Mater.* **2010**, *22*, 4712–4720.
- (6) Adzic, R. R.; Zhang, J.; Sasaki, K.; Vukmirovic, M. B.; Shao, M. H.; Wang, J. X.; Nilekar, A. U.; Mavrikakis, M.; Valerio, J. A.; Uribe, F. *Top. Catal.* **2007**, *46*, 249–262.
- (7) Ozaki, J.; Anahara, T.; Kimura, N.; Oya, A. *Carbon* **2006**, *44*, 3358–3361.
- (8) Lefèvre, M.; Proietti, E.; Jaouen, F.; Dodelet, J.-P. *Science* **2009**, *324*, 71–74.
- (9) Gong, K. P.; Du, F.; Xia, Z. H.; Durstock, M.; Dai, L. M. *Science* **2009**, *323*, 760–764.
- (10) Liu, R. L.; Wu, D. Q.; Feng, X. L.; Müllen, K. *Angew. Chem., Int. Ed.* **2010**, *49*, 2619–2623.
- (11) Wu, G.; More, K. L.; Johnston, C. M.; Zelenay, P. *Science* **2011**, *332*, 443–447.
- (12) Geng, D.; Chen, Y.; Chen, Y. G.; Li, Y.; Li, R.; Sun, X.; Ye, S.; Knights, S. *Energy Environ. Sci.* **2011**, *4*, 760–764.
- (13) Jo, G.; Shanmugam, S. *Electrochem. Commun.* **2012**, *25*, 101–104.
- (14) Yang, L. J.; Jiang, S. J.; Zhao, Y.; Zhu, L.; Chen, S.; Wang, X. Z.; Wu, Q.; Ma, J.; Ma, Y. W.; Hu, Z. *Angew. Chem., Int. Ed.* **2011**, *50*, 7132–7135.
- (15) Daems, N.; Sheng, X.; Vankelecom, I. F. J.; Pescarmona, P. P. *J. Mater. Chem. A* **2014**, *2*, 4085–4110.
- (16) Wang, H.; Bo, X. J.; Zhang, Y. F.; Guo, L. P. *Electrochim. Acta* **2013**, *108*, 404–411.
- (17) Inamdar, S.; Choi, H.-S.; Wang, P.; Song, M. Y.; Yu, J.-S. *Electrochem. Commun.* **2013**, *30*, 9–12.
- (18) Liu, Z. W.; Peng, F.; Wang, H. J.; Yu, H.; Zheng, W. X.; Yang, J. *Angew. Chem., Int. Ed.* **2011**, *50*, 3257–3261.
- (19) Yang, D.-S.; Bhattacharjya, D.; Inamdar, S.; Park, J.; Yu, J.-S. *J. Am. Chem. Soc.* **2012**, *134*, 16127–16130.
- (20) Li, R.; Wei, Z. D.; Gou, X. L.; Xu, W. *RSC Adv.* **2013**, *3*, 9978–9984.
- (21) Xu, J. X.; Guan, L. H. *RSC Adv.* **2013**, *3*, 5577–5582.
- (22) Roy, R. K.; Shen, S.; Kernion, S. J.; McHenry, M. E. *J. Appl. Phys.* **2012**, *111*, 07A301.
- (23) Wu, J.; Yang, Z. R.; Li, X. W.; Sun, Q. J.; Jin, C.; Strasser, P.; Yang, R. Z. *J. Mater. Chem. A* **2013**, *1*, 9889–9896.
- (24) Zhang, M.; Dai, L. M. *Nano Energy* **2012**, *1*, 514–517.
- (25) Zhang, L. P.; Xia, Z. H. *J. Phys. Chem. C* **2011**, *115*, 11170–11176.
- (26) Yang, Z.; Yao, Z.; Li, G. F.; Fang, G. Y.; Nie, H. G.; Liu, Z.; Zhou, X. M.; Chen, X. A.; Huang, S. M. *ACS Nano* **2012**, *6*, 205–211.
- (27) Yu, D. S.; Xue, Y. H.; Dai, L. M. *J. Phys. Chem. Lett.* **2012**, *3*, 2863–2870.

- (28) Choi, C. H.; Park, S. H.; Woo, S. I. *ACS Nano* **2012**, *6*, 7084–7091.
- (29) Wu, J.; Yang, Z. R.; Wang, Z. J.; Sun, Q. J.; Yang, R. Z. *Electrochem. Commun.* **2014**, *42*, 46–49.
- (30) Von Deak, D.; Biddinger, E. J.; Luthman, K. A.; Ozkan, U. S. *Carbon* **2010**, *48*, 3637–3639.
- (31) Wang, S.; Yu, D.; Dai, L.; Chang, D. W.; Baek, J. B. *ACS Nano* **2011**, *5*, 6202–6209.
- (32) Hu, C. Y.; Yang, D.-P.; Zhu, F. J.; Jiang, F. J.; Shen, S. Y.; Zhang, J. L. *ACS Appl. Mater. Interfaces* **2014**, *6*, 4170–4178.
- (33) Hu, C. Y.; Yang, D.-P.; Wang, Z. Y.; Yu, L. L.; Zhang, J. L.; Jia, N. Q. *Anal. Chem.* **2013**, *85*, 5200–5206.
- (34) Sunarso, J.; Torriero, A. A.; Zhou, W.; Howlett, P. C.; Forsyth, M. *J. Phys. Chem. C* **2012**, *116*, 5827–5834.
- (35) Markovic, N. M.; Gasteiger, H.; Ross, P. N. *J. Phys. Chem.* **1996**, *100*, 6715–6721.
- (36) Wu, J.; Yang, Z. R.; Sun, Q. J.; Li, X. W.; Strasser, P.; Yang, R. Z. *Electrochim. Acta* **2014**, *127*, 53–60.
- (37) Liang, Y. Y.; Wang, H. L.; Zhou, J. G.; Li, Y. G.; Wang, J.; Regier, T.; Dai, H. J. *J. Am. Chem. Soc.* **2012**, *134*, 3517–3523.
- (38) Du, J.; Pan, Y. D.; Zhang, T. R.; Han, X. P.; Cheng, F. Y.; Chen, J. J. *Mater. Chem.* **2012**, *22*, 15812–15818.
- (39) Markovic, N. M.; Schmidt, T. J.; Stamkovic, V. S.; Ross, P. N. *Fuel cells* **2001**, *1*, 105–116.
- (40) Shirley, D. A. *Phys. Rev. B* **1972**, *5*, 4709–4714.
- (41) Briggs, D.; Seah, M. P. Practical surface analysis, In *Auger and X-ray photoelectron spectroscopy*, 2nd ed.; Wiley-Interscience: New York, 1990; Vol. 1, pp 87–139.
- (42) Tian, X. Y.; He, W.; Cui, J. J.; Zhang, X. D.; Zhou, W. J.; Yan, S. P.; Sun, X. N.; Han, X. X.; Han, S. S.; Yue, Y. Z. *J. Colloid Interface Sci.* **2010**, *343*, 344–349.
- (43) Du, X. Y.; He, W.; Zhang, X. D.; Yue, Y. Z.; Liu, H.; Zhang, X. G.; Min, D. D.; Ge, X. X.; Du, Y. J. *Mater. Chem.* **2012**, *22*, 5960–5969.
- (44) Liang, J.; Du, X.; Gibson, C.; Du, X. W.; Qiao, S. Z. *Adv. Mater.* **2013**, *25*, 6226–6231.
- (45) Yang, R. Z.; Bonakdarpour, A.; Easton, E. B.; Stoffyn-Egli, P.; Dahn, J. R. *J. Electrochem. Soc.* **2007**, *154*, A275–282.
- (46) Dake, L. S.; Baer, D. R.; Friedrich, D. M. *J. Vac. Sci. Technol. A* **1989**, *7*, 1634–1638.
- (47) Paraknowitsch, J. P.; Zhang, Y. J.; Wienert, B.; Thomas, A. *Chem. Commun.* **2013**, *49*, 1208–1210.
- (48) Wu, J.; Jin, C.; Yang, Z. R.; Tian, J. H.; Yang, R. Z. *Carbon* **2015**, *82*, 562–571.
- (49) Yang, R. Z.; Stevens, K.; Bonakdarpour, A.; Dahn, J. R. *J. Electrochem. Soc.* **2007**, *154*, B893–B901.
- (50) Yang, R. Z.; Stevens, K.; Easton; Dahn, J. R. *J. Electrochem. Soc.* **2008**, *155*, B79–B91.
- (51) Xing, W.; Xue, J. S.; Dahn, J. R. *J. Electrochem. Soc.* **1996**, *143*, 3046–3052.
- (52) Wang, Q.; Li, H.; Huang, X. J.; Chen, L. Q. *Carbon* **2001**, *39*, 2211–2214.
- (53) Jiang, H.; Zhu, Y.; Feng, Q.; Su, Y.; Yang, X.; Li, C. *Chem. Eur. J.* **2014**, *20*, 3106–3112.
- (54) Li, J.; Li, S.; Tang, Y.; Li, K.; Zhou, L.; Kong, N.; Lan, Y.; Bao, J.; Dai, Z. *Sci. Rep.* **2014**, *4*, 5130.
- (55) Jiang, L.; Hsu, A.; Chu, D.; Chen, R. *J. Electrochem. Soc.* **2009**, *156*, B370–376.
- (56) Yang, W.; Fellingner, T.-P.; Antonietti, M. *J. Am. Chem. Soc.* **2011**, *133*, 206–209.
- (57) Yang, Z. R.; Wu, J.; Zheng, X. J.; Wang, Z. J.; Yang, R. Z. *J. Power Sources* **2015**, *277*, 161–168.